Relationship between Fill Factor and Light Intensity in Solar Cells Based on Organic Disordered Semiconductors: The Role of Tail States

Biao Xiao,[1] Philip Calado,[2] Roderick C.I. MacKenzie,[3] Thomas Kirchartz,[4,5] Jun Yan[2,*] and Jenny Nelson[2]

[1]*Key Laboratory of Optoelectronic Chemical Materials and Devices, Ministry of Education, Flexible Display Materials and Technology Co-Innovation Centre of Hubei Province, School of Chemical and Environmental Engineering, Jianghan University, Wuhan 430056, China*

[2]*Department of Physics and Centre for Plastic Electronics, Imperial College London, London SW7 2AZ, United Kingdom*

[3]*Faculty of Engineering, University of Nottingham, University Park, Nottingham NG7 2RD, United Kingdom*

[4]*IEK5-Photovoltaics, Forschungszentrum Jülich, Jülich 52425, Germany*

[5]*Faculty of Engineering and CENIDE, University of Duisburg-Essen, Carl-Benz-Str. 199, Duisburg 47057, Germany*

The origin of the relationship between fill factor (FF) and light intensity (I) in organic disordered-semiconductor-based solar cells is studied. An analytical model describing the balance between transport and recombination of charge carriers, parameterized with a factor, Γ_m, is introduced to understand the FF-I relation, where higher values of Γ_m correlate to larger FFs. Comparing the effects of direct and tail-state-mediated recombination on the FF-I plot, we find that, for low-mobility systems, direct recombination with constant transport mobility can deliver only a negative dependence of $\Gamma_{m,\mathrm{dir}}$ on light intensity. By contrast, tail-state-mediated recombination with trapping and detrapping processes can produce a positive $\Gamma_{m,t}$ versus sun dependency. The analytical model is validated by numerical drift-diffusion simulations. To further validate our model, two material systems that show opposite FF-I behavior are studied: poly{4,8-bis[5-(2-ethylhexyl)thiophen-2-yl]benzo[1,2-*b*;4,5-*b′*]dithiophene-2,6-diyl-*alt*-[4-(2-ethylhexyl)-3-fluorothieno[3,4-*b*]thiophene)-2-carboxylate-2-6-diyl]} (PTB7-Th):[6,6]-phenyl-C$_{71}$-butyric acid methyl ester (PC$_{71}$BM) devices show a negative FF-I relation, while PTB7-Th:(5Z,5′Z)-5,5′-{[7,7′ -(4,4,9,9-tetraoctyl-4,9-dihydro-*s*-indaceno[1,2-*b*:5,6-*b′*]dithiophene-2,7-diyl)bis(benzo[*c*][1,2,5]thiadiazole-7,4-diyl)]bis(methanylylidene)}bis(3-ethyl-2-thioxothiazolidin-4-one) (O-IDTBR) devices show a positive correlation. Optoelectronic measurements show that the O-IDTBR device presents a higher ideality factor, stronger trapping and detrapping behavior, and a higher density of trap states, relative to the PC$_{71}$BM device, supporting the theoretical model. This work provides a comprehensive understanding of the correlation between FF and light intensity for disordered-semiconductor-based solar cells.

I. INTRODUCTION

Organic semiconductors [1–5] are widely studied material systems for photovoltaic applications, due to their ease of processing, chemical tunability, low cost, flexibility, and low weight. However, as the materials are intrinsically disordered, they often have lower mobilities and increased density of trap states, relative to more ordered semiconductors [6]. Consequently, when used as active materials for thin-film photovoltaics, the competition between charge-carrier extraction and charge recombination is a key concern affecting the magnitude of the photogenerated current density at operating point. These losses often result in a reduction in the current density-voltage (*J-V*) curve fill factor (FF) of devices. The FF is determined by the ratio between maximum power generated, which is the product of the current density (J_m) and voltage (V_m) at maximum power point (MPP), and the product of short-circuit current density (J_{SC}) with the open-circuit voltage (V_{OC}), such that [7]

$$\mathrm{FF} = \frac{J_m V_m}{J_{\mathrm{SC}} V_{\mathrm{OC}}}. \qquad (1)$$

The performance of a photovoltaic device is therefore related to FF through $\eta = J_{\mathrm{SC}} V_{\mathrm{OC}} \mathrm{FF}/P_s$, where η is the

———————
*j.yan17@imperial.ac.uk

power conversion efficiency and P_s is the incident-light power density [7]. Therefore, to maximize η, a high FF is required.

Measuring the current-voltage characteristics at 1 sun characterizes the devices under standard solar illumination. Understanding device responses at lower light intensities is important for determining annual energy-conversion yields and, in particular, for indoor photovoltaics [8,9]. Additionally, studying light-intensity-dependent performance can provide an insight into loss mechanisms in devices [10,11]. However, the majority of studies based on light-intensity-dependent performance measurements are focused on either V_{OC} [10,12,13] or J_{SC} [10,11,14]. Only a limited number have investigated FF [15], owing to the difficulty in describing its physical origins and accounting for the many factors that contribute to it.

In most of those studies based on organic solar cells, FF is shown to decrease with increasing light intensity. [16–21] A small number of studies, however, have shown the reverse, namely, that FF increases with light intensity for intensities below 1 sun [15,22]. The first type of behavior is rationalized by either a superlinear increase in the bimolecular recombination rate with charge density, and hence, light intensity [21], or series resistive effects [23]. In the second type of behavior, where FF increases with increasing light intensity, the reasons are less clear. Researchers have proposed that the leakage current due to a low shunt resistance in organic solar cells (OSCs) [15,23] controls the FF under low light intensity, resulting in a reduction of FF at very low light intensities (less than 10^{-5} sun) [15,23]. However, the leakage current cannot easily be differentiated from the dark saturation current [24,25], making it difficult to extract key information solely from the shunt resistance values measured using the dark current. At present, no complete model exists to explain these two types of behavior.

The FF of low-mobility semiconductor-based solar cells has been correlated to competition between charge recombination and charge extraction [26,27], with the earliest study dating back to 1932 by Hecht [28]. Bartesaghi *et al.* [29] adapted this concept and applied it to organic solar cells successfully. The concept was later used to derive analytical expressions for the *J-V* curve of a low-mobility diode [30] and was extended [31] to take recombination mechanisms, space-charge effects, and contacts into account. All of these models are successfully applied to OSCs under standard solar illumination (1 sun). At lower light intensities, however, the carrier-density dependence of transport and recombination processes becomes more important and is expected to affect the FF-*I* relation. Considering the disordered nature of OSCs, caused by the distribution of conjugation lengths, disorder in conformation, crystallinity, etc., the extended density of electronic states (DOS) and the associated dispersive charge transport and recombination processes must be included in any analysis

that aims to explain the behavior of the FF over orders of magnitude in light intensity.

Here, we derive an analytical model to describe the correlation between FF and light intensity in organic disordered-semiconductor-based solar cells. We consider separately the effects of direct and trap-mediated recombination on the FF-*I* plot. Our analytical models are verified using a more complex one-dimensional numerical drift-diffusion simulation based on the general purpose photovoltaic device model (gpvdm) software [32,33]. Our results suggest that, for low-mobility systems, devices that are limited by direct recombination always show a negative dependence of FF on light intensity, while devices with tail states can show the opposite behavior. To test the proposed model, we study two different types of organic blend device that show different FF-*I* relationships, one based on a poly{4,8-bis[5-(2-ethylhexyl)thiophen-2-yl)benzo[1,2-*b*;4,5-*b′*]dithiophene-2,6-diyl-*alt*-[4-(2-ethyl hexyl)-3-fluorothieno[3,4-*b*]thiophene)-2-carboxylate-2-6-diyl]} (PTB7-Th) [34]:[6,6]-phenyl-C$_{71}$-butyric acid methyl ester (PC$_{71}$BM) absorber layer and the other (PTB7-Th:O-IDTBR) using the nonfullerene acceptor (5Z,5′Z)-5,5′-{[7,7′ -(4,4,9,9-tetraoctyl-4,9-dihydro-*s*-ind-aceno[1,2-*b*:5,6-*b′*]dithiophene-2,7-diyl)bis(benzo[*c*][1,2,5]thiadiazole-7,4-diyl)]bis(methanylylidene)}bis(3-ethyl-2-thioxothiazolidin-4-one) (O-IDTBR) [35,36] instead of the fullerene PC$_{71}$BM. The theoretical analysis is supported by experimental estimation of the trap states in the two device types. The PTB7-Th:O-IDTBR device is shown to have a higher ideality factor, stronger trapping and detrapping behavior, and higher trap density than those of the PC$_{71}$BM device, leading to a positive FF-*I* relation, as opposed to the negative relation shown in the PC$_{71}$BM device.

II. THEORY AND MODEL

The FF of a classical inorganic solar cell depends on the two resistive elements of the standard equivalent circuit of a solar cell, namely, the series and parallel resistance (R_s and R_p) [37]. In addition, the voltage dependence of the recombination current J_{rec} matters. This voltage dependence is approximately exponential, scaling with $J_{rec} \sim \exp[qV/(n_{id}k_BT)]$, where k_BT/q is the thermal voltage and n_{id} is the ideality factor that provides information about the dominant recombination mechanism [38,39]. Several studies have discussed how resistive effects and recombination mechanisms change the relationship between fill factor and light intensity using the diode equation, which we call the FF-*I* relationship [40,41]. In the absence of resistive effects and recombination through trap states, the FF should depend on light intensity in a similar way to V_{OC}, i.e., increased light intensity results in a higher V_{OC} and FF [37,40]. Series resistance losses, however, increase with increasing current density and may cause

an associated decrease in the FF with higher light intensities. The addition of trap recombination or shunt resistances may result in an increase of the FF with light intensity [40]. However, these insights are based on the standard equivalent circuit model of a solar cell under illumination and do not account for disorder or inefficient charge collection.

In the case of disordered organic or inorganic absorber materials, low mobilities are generally undesirable. Hence, to compensate for the effects of low mobilities, the device design of disordered organic or inorganic materials is typically chosen such that the absorber layer is fully or nearly fully depleted. For low-mobility-lifetime products, the wide field-bearing depletion zone helps to achieve efficient charge extraction, relative to a partially depleted design [42]. The electric field in a fully depleted organic solar cells is approximately given by $(V_{BI} - V)/d$, where V_{BI} is the built-in potential, V is the applied voltage, and d is the active layer thickness. Because the electric field affects the probability of charge collection [26,27], the recombination current can be voltage and illumination dependent, as opposed to the standard equivalent circuit description of a solar cell, and consequently, the superposition principle [43] can no longer be applied. Instead, a range of different effects may influence the light-intensity dependence of the fill factor. These have been described variously as light-intensity- and voltage-dependent photocurrents [26,27], recombination currents [21], internal series resistances [44], or even ideality factors [45], all of which may modify the device current-voltage curve.

Previous modeling studies [29–31] had great success in understanding the limitations on FF under 1 sun. For example, a study by Koster and co-workers [29] introduced a factor, θ, representing the recombination-to-extraction rate at short circuit as a way to quantify collection efficiency and indicate FF. This approach is referred to as the Koster model in this paper. However, previous analyses have not considered the impact of charge-carrier-density-dependent carrier mobility [46,47] nor have they considered the situation at maximum power point. Thus, an adapted analysis is required to properly model disordered systems with significant densities of tail states.

In the model described herein, we compare cases with and without carrier-density-dependent charge transport. We begin by considering two types of recombination present in real-world solar cells (rather than assuming only Langevin-type second-order recombination [29]):

(1) Second-order direct free-electron-to-free-hole recombination with no trap-mediated recombination and constant mobility.

(2) First-order trap-mediated recombination and transport, as they are often seen as the dominating loss mechanism in OSCs [33,48–51].

We model a device directly at the MPP, under the assumption that V_m is proportional to V_{OC}. This is validated numerically using gpvdm [32,33] (see Fig. S8 within the Supplemental Material [52]) and is often the case for real-world OSCs [53]. It follows that V_m can be expressed as a constant fraction (w) of V_{OC} ($w < 1$), such that

$$V_m = wV_{OC}. \quad (2)$$

We consider a uniform absorption profile and charge transport to be drift dominated at the MPP. We also assume that quasi-Fermi levels are spatially invariant at the MPP. We parameterize the model using the transport-to-recombination factor at the MPP, Γ_m. In the model, we define Γ_m as the ratio between the drift transport (K_{dr}) and recombination (K_{rec}) rate constants (both in the units of s^{-1}), such that $\Gamma_m = K_{dr}/K_{rec}$. For interest, we compare our approach with that taken by Koster and co-workers [29] in Table S1 within the Supplemental Material [52].

A. A model for devices dominated by direct second-order recombination without tail states

Direct recombination occurs between a free electron and a free hole and can be radiative [54], as illustrated in Fig. 1. For the purpose of this analysis, let us imagine a simple one-dimensional device with symmetric electron and hole distributions, transport, and recombination processes. Assuming the averaged quasi-Fermi-level splitting across the device equals applied voltage, i.e., $\overline{\Delta E_F} = qV$, the averaged direct recombination rate [$R_{rec,dir}(V)$] can be expressed as a function of the applied voltage (V) via [7]

$$R_{rec,dir}(V) = B_{dir}N_C N_V \exp\left(\frac{qV - E_g}{k_B T}\right) = k_{dir}n_f{}^2, \quad (3)$$

where N_C and N_V are the effective density of states for the donor material conduction band and the acceptor material valence band, respectively; k_B is the Boltzmann constant; T is the temperature; B_{dir} is the direct recombination coefficient; n_f is the free-electron density ($n_f = p_f$); and E_g is the effective band gap of the blend set to be equal to the product of the elementary charge (q) and the built-in potential V_{BI}, based on the fact that, for most efficient OSCs, the contacts match with the HOMO of the donor and the LUMO of the acceptor. In Eq. (3), we neglect the dark generation term based on the assumption that it is much smaller than the generation rate under the range of illumination intensities of interest. Using Eq. (3), we can relate the recombination rate at the MPP to the rate at OC, and therefore, to the light intensity (I), via

$$\begin{aligned} R_{rec,dir}(V_m) &= R_{rec,dir}(V_{OC,dir}) \exp\left[-\frac{(1-w)qV_{OC,dir}}{k_B T}\right] \\ &= C_G I \exp\left[-\frac{(1-w)qV_{OC,dir}}{k_B T}\right]. \quad (4) \end{aligned}$$
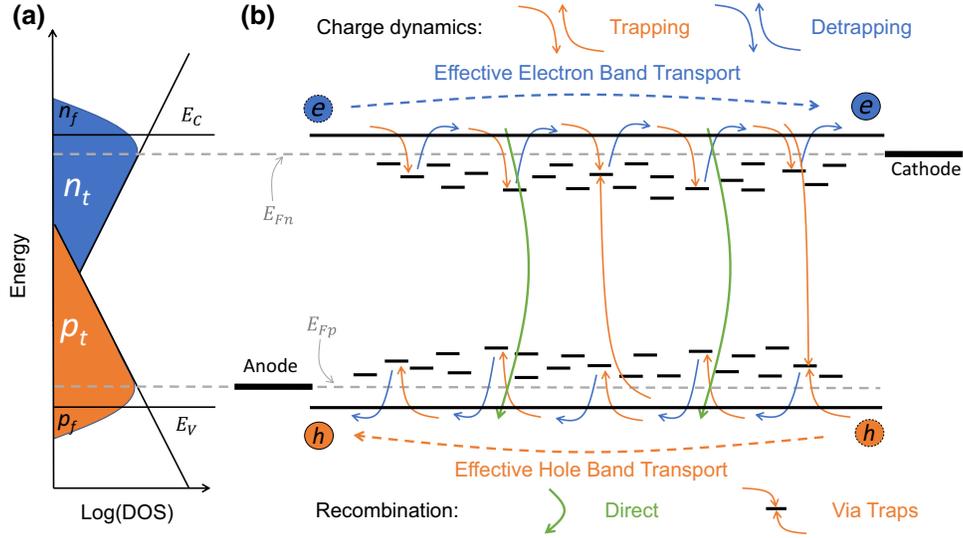
FIG. 1. Illustration of (a) the DOS and (b) direct recombination, recombination through tail states, and charge transport with multiple trapping and detrapping processes, assuming an exponential-type density of tail states under flat-band condition. This is an assumption that MPP condition is close to flat-band condition [open-circuit (OC) condition]. Free charge densities (n_f, p_f), and trapped charge densities (n_t, p_t) are given by the integral of Fermi-Dirac distribution function with the DOS [82]). See Sec. IV within the Supplemental Material for details [52].

At OC, the average volumetric rate of direct recombination $R_{\text{rec,dir}}(V_{\text{OC,dir}})$ is balanced by the average volumetric generation rate $R_{\text{rec,dir}}(V_{\text{OC,dir}}) = G = C_G I$, and C_G is the generation rate at 1 sun illumination. The open-circuit voltage ($V_{\text{OC,dir}}$) depends linearly on the effective band gap, E_g, and logarithmically on light intensity (I) (see Sec. III within the Supplemental Material for details [52]), via

$$V_{\text{OC,dir}} = \frac{E_g}{q} - \frac{k_B T}{q} \ln\left(\frac{B_{\text{dir}} N_C N_V}{C_G I}\right). \quad (5)$$

With an ideality factor, $n_{\text{id,dir}}$, of one, the free charge-carrier density at the MPP ($n_{f,m}$) can then be expressed as

$$n_{f,m} = \sqrt{\frac{C_G I}{B_{\text{dir}}}} \exp\left[-\frac{(1-w)q V_{\text{OC,dir}}}{2 k_B T}\right]. \quad (6)$$

We can then describe a pseudo-first-order recombination rate "constant," $K_{\text{rec,dir}}(n_f)$ (s^{-1}), for which $R_{\text{rec,dir}}(V) = K_{\text{rec,dir}}(n_f)n_f = n_f/\tau_{\text{dr}}$. At the MPP, we have

$$K_{\text{rec,dir}}(V_m) = \sqrt{B_{\text{dir}} C_G I} \exp\left[-\frac{(1-w)q V_{\text{OC,dir}}}{2 k_B T}\right]. \quad (7)$$

At the MPP, we assume that carrier transport is drift dominated, which should be valid provided that $V_m < V_{\text{BI}}$ and a large enough electric field is maintained [42]. We use the drift rate coefficient (s^{-1}), $K_{\text{dr,dir}}(V_m)$, as a proxy for the extraction rate coefficient at the MPP to describe the

average rate for carriers to drift to the respective contacts [29]:

$$K_{\text{dr,dir}}(V_m) = \frac{\mu(V_{\text{int,}m}/L)}{(L/2)} = \frac{2\mu V_{\text{int,}m}}{L^2}. \quad (8)$$

Here, μ is the constant transport mobility (we assume balanced electron and hole mobilities), L is the layer thickness, and $V_{\text{int,}m}$ is the internal electrostatic potential drop across the absorber layer at the MPP. The internal voltage, $V_{\text{int,}m}$, is given by

$$V_{\text{int,}m} = V_{\text{BI}} - V_m = V_{\text{BI}} - w V_{\text{OC,dir}}. \quad (9)$$

The transport-to-recombination factor for direct recombination, $\Gamma_{m,\text{dir}}$, is then

$$\Gamma_{m,\text{dir}} = \frac{K_{\text{dr,dir}}(V_m)}{K_{\text{rec,dir}}(V_m)} = \frac{2\mu}{L^2 \sqrt{B_{\text{dir}} C_G}}$$
$$\times \frac{V_{\text{BI}} - w V_{\text{OC,dir}}}{\exp\left[-\frac{(1-w)q V_{\text{OC,dir}}}{2 k_B T}\right]} \times \frac{1}{\sqrt{I}} \propto \frac{V_{\text{BI}} - w V_{\text{OC,dir}}}{I^{\left(w - \frac{1}{2}\right)}}. \quad (10)$$

Since $V_{\text{OC,dir}}$ is proportional to the log of the light intensity (I) in Eq. (10), i.e., $V_{\text{OC,dir}} \propto \ln(I)$, $\Gamma_{m,\text{dir}}$ should decrease with light intensity I, as long as $w > 1/2$ is assured (common for practical devices), indicating that direct recombination can deliver only a negative dependence between $\Gamma_{m,\text{dir}}$ and I, and hence, a negative dependence of FF on light intensity. This relationship shows

that, if the device is limited by direct recombination, FF tends to higher values at lower light intensities, as is often reported for high-efficiency devices [18,34]. We expect the same result using the Koster model [29], since in that model factor θ is proportional to the generation rate (equivalent to light intensity) and the mobility is constant. Therefore, the model devices limited by direct recombination and constant mobility cannot produce a positive FF-I correlation.

B. A model for devices dominated by tail-state-mediated recombination

Tail-state models have often been used to understand unusual behavior in OSCs [33,48,49] and, as discussed above, are essential to a comprehensive model of devices operating at low light intensity. As we show in this section, only a model including trap-mediated recombination and trap-mediated transport can reproduce the positive FF dependence on light intensity described in Sec. I.

This approach is motivated by two key observations in the field of OSCs, i.e., (1) most devices present ideality factors greater than one [55,56]; and (2) a Langevin-type second-order bimolecular recombination mechanism, which is defined by $R = B_L np$, seldom holds [57,58], where $B_L = \frac{q}{\varepsilon_0 \varepsilon_r}(\mu_n + \mu_p)$; ε_0 is the vacuum permittivity; ε_r is the relative permittivity of the blend; and μ_n and μ_p are the electron and hole mobility, respectively. These observations lead to the following assumptions:

(1) The DOS of organic semiconductors is distributed in energy and follows an exponential-type distribution function.

(2) Charge transport is correlated to charge-carrier density through trapping and detrapping processes, as opposed to the carrier-density-independent mobility approximation that is commonly used [29].

Figure 1 is a schematic showing charge-carrier occupation and transport in an extended exponential-type DOS based on the concept of multiple trapping and detrapping. As with the direct recombination analysis, we consider a one-dimensional device with symmetric charge-carrier distributions, transport, and recombination. In the trap-mediated recombination model, recombination primarily occurs between free charges and trapped charges. Hence, the average volumetric recombination rate, $R_{\text{rec},t}(V)$, can be expressed as [39]

$$R_{\text{rec},t}(V) = B_t n_f p_t, \tag{11}$$

where B_t is a constant prefactor, n_f is the free charge-carrier density, and p_t is the trapped carrier density, and we neglect the small contribution from dark generation. We assume that the capture coefficients of the conduction-band tail from the conduction band are much larger than the capture coefficients of the conduction-band tail with the valence band (and vice versa), such that the trapped carriers are in equilibrium with free carriers in each band, i.e., the free and trapped charges in each band share the same quasi-Fermi levels. (We note that this assumption is not required in the numerical modeling presented later.) Assuming an identical exponential tail for both conduction and valence bands, the density of trapped (holes) and free carriers (electrons) can be estimated as [59,60]

$$p_t = n_t \approx N_t \exp\left(-\frac{\Delta E_F}{E_t}\right), \tag{12a}$$

$$n_f = N_C \exp\left(-\frac{\Delta E_F}{k_B T}\right). \tag{12b}$$

Here, N_t is the total density of localized trap states determined by $E_t U_t^{\text{exp}}$, where U_t^{exp} is the effective density of trap states per unit energy [33] with the units of $\text{m}^{-3}\,\text{eV}^{-1}$ and E_t is the characteristic energy of the exponential tail. ΔE_F is the relative position of the quasi-Fermi potential to the conduction band for electrons: $\Delta E_F = E_C - E_{\text{FN}} = E_{\text{FP}} - E_V = (1/2)(E_g - qV)$, E_C and E_V are the energy of the conduction- and valence-band edges, E_{FN} and E_{FP} are the internal quasi-Fermi level for electrons and holes, respectively. A detailed derivation for free and trapped charge densities, and a discussion on the validity of Eq. (12a) can be found in the Supplemental Material [52]. Using Eq. (12), we can rewrite the equation for the hole density in the valence-band tail as a function of free electron density in the conduction band:

$$p_t = n_t = N_t \left(\frac{n_f}{N_C}\right)^{k_B T / E_t}. \tag{13}$$

By substituting Eq. (13) into Eq. (11) we obtain

$$R_{\text{rec},t}(V) = \frac{B_t N_t}{N_C^{k_B T / E_t}} n_f^{(k_B T / E_t + 1)}. \tag{14}$$

So, we have the reaction order for free charge carriers, $\Delta = k_B T / E_t + 1$, as previously derived by Kirchartz and Nelson [39]. Hence, E_t is directly related to the reaction order (Δ) within this framework. The pseudo-first-order recombination rate coefficient $K_{\text{rec},t}(n_f)$ (s^{-1}), for which $R_{\text{rec},t}(V) = K_{\text{rec},t}(n_f)n_f = n_f / \tau_t$, at the MPP is then

$$K_{\text{rec},t}(V_m) = \frac{B_t N_t}{N_C^{(\Delta-1)}} n_{f,m}^{(\Delta-1)} = \frac{B_t N_t}{N_C^{(\Delta-1)}} n_{f,\text{OC}}^{(\Delta-1)}$$

$$\times \exp\left[-\frac{(\Delta-1)(1-w)qV_{\text{OC},t}}{2k_B T}\right]. \tag{15}$$

Here, the open-circuit voltage ($V_{OC,t}$) is given by (see the Supplemental Material for details [52])

$$V_{OC,t} = \frac{E_g}{q} - \frac{n_{id,t}k_B T}{q}\ln\left(\frac{B_t N_t N_C}{C_G I}\right), \quad (16)$$

The ideality factor $n_{id,t}$ is defined by assuming the same characteristic energy for both conduction and valance bands (see the Supplemental Material for the derivation [52]):

$$n_{id,t} = \frac{2}{1 + \frac{k_B T}{E_t}} = \frac{2}{\Delta}. \quad (17)$$

The free charge density at OC ($n_{f,OC}$) can be directly related to the light intensity (I) based on the fact that, at open circuit, $R_{rec,t}(V_{OC,t}) = G = C_G I$ through

$$n_{f,OC} = \left[\frac{IC_G N_C^{(\Delta-1)}}{B_t N_t}\right]^{1/\Delta}. \quad (18)$$

Hence, the free charge-carrier density at the MPP ($n_{f,m}$) can be expressed as

$$n_{f,m} = \left[\frac{IC_G N_C^{(\Delta-1)}}{B_t N_t}\right]^{1/\Delta}\exp\left[-\frac{(1-w)qV_{OC,t}}{2k_B T}\right]. \quad (19)$$

Following the same method as that in Sec. II A, we assume that the carrier drift rate coefficient, $K_{dr,t}(V_m)$, parameterizes the charge-transport rate at the MPP for electrons [42]. However, the multiple trapping model requires that we substitute the mobility term for an effective mobility, μ_{eff}:

$$K_{dr,t}(V_m) = \frac{2\mu_{eff}V_{int,t}}{L^2}. \quad (20)$$

Where $V_{int,t}$ follows Eq. (9) with $V_{OC,dir}$ replaced by $V_{OC,t}$. In the presence of trapping and detrapping processes, the effective band mobility (μ_{eff}) is determined by the ratio between free charges (n_f) and total charges ($n_f + n_t$) through [48]

$$\mu_{eff} = \mu_0 \frac{n_f}{n_f + n_t}, \quad (21)$$

where μ_0 is the trap-free mobility. At the MPP, Eq. (21) becomes

$$\mu_{eff,m} = \mu_0 \frac{1}{1 + N_t N_C^{(1-\Delta)}n_{f,m}^{(\Delta-2)}}. \quad (22)$$

Finally, we obtain the transport-to-recombination factor for tail-state-mediated recombination ($\Gamma_{m,t}$):

$$\Gamma_{m,t} = \frac{K_{dr,t}(V_m)}{K_{rec,t}(V_m)}$$

$$= \frac{2\mu_0(V_{BI} - wV_{OC,t})}{L^2 B_t N_t N_C^{(1-\Delta)}[n_{f,m}^{(\Delta-1)} + N_t N_C^{(1-\Delta)}n_{f,m}^{(2\Delta-3)}]}. \quad (23)$$

Note that we express $\Gamma_{m,t}$ as a function of $n_{f,m}$ for better readability, since $n_{f,m}$ is positively dependent on the light intensity (I). In Eq. (23), the numerator has a negative but weak dependence on light intensity, such that the term in the denominator dominates the relationship between I and $\Gamma_{m,t}$. The first term in the square brackets of the denominator can only result in a negative dependence of $\Gamma_{m,t}$ on I (negative FF-I dependence), since the reaction order is always greater than one ($\Delta > 1$) and $n_{f,m}$ increases with light intensity. The second term in the denominator can, however, result in a positive dependence of $\Gamma_{m,t}$ on I (positive FF-I dependence) for values of $\Delta < 1.5$. This corresponds to characteristic trap energies of $E_t > 2k_B T$ (approximately 52 meV at 300 K). This result implies that the reaction order is critical to defining the FF-I behavior, and devices with higher reaction orders close to two are less likely to have a positive FF-I relation. The balance of these terms is also determined by the balance of the normalized generation rate, C_G, to the trap-mediated rate coefficient, B_t, and the total trap density, N_t, to the effective density of band states, N_C. Results from the analytical model using realistic parameters are presented in Sec. III B 2.

III. MODEL RESULTS: ANALYTICAL VERSUS NUMERICAL

In this section, analytical model results of FF versus Γ_m are compared with numerical drift-diffusion simulations performed using gpvdm [32,33]. Comparisons are carried out first at 1 sun illumination, then over a range of different illumination intensities.

A. Comparison of the analytical and numerical models at 1 sun illumination

We first perform calculations using the proposed analytical model [Eqs. (10) and (23)] under 1 sun using a large parameter space, to obtain a comprehensive picture of the correlation between FF and $\Gamma_{m,dir}$ and between FF and $\Gamma_{m,t}$. Figures S3 and S5 within the Supplemental Material [52] show that there is minimal impact on the Γ_m versus I relation with different values of w. We therefore fix $w = 0.8$ for the remainder of the analysis. For direct recombination, the mobility (μ) and recombination constant (B_{dir}) are varied using ranges of 10^{-5} to
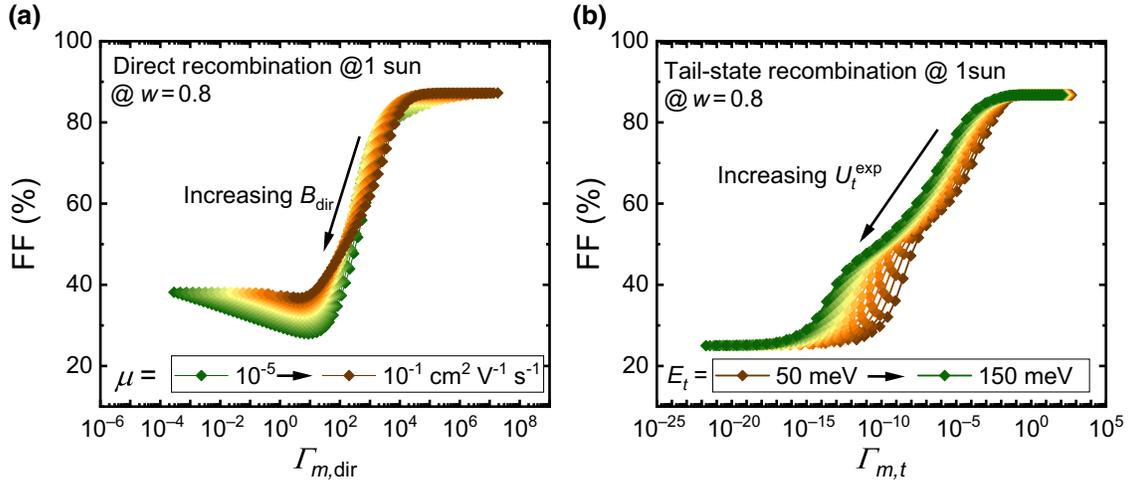
FIG. 2.   FF as a function of Γ_m at 1 sun illumination with $w = 0.8$. (a) Direct recombination with varied bimolecular recombination constant ($B_{\mathrm{dir}} = 10^{-20} - 10^{-8}$ m^{-3} s^{-1}) and mobility ($\mu = 10^{-5} - 10^{-1}$ cm^2 V^{-1} s^{-1}). (b) Trap-mediated recombination with a varying characteristic energy ($E_t = 0.05 - 0.15$ eV) assigned to the model, along with trap densities (U_t^{exp}) varying from 10^{15} to 10^{28} m^{-3} eV^{-1}. Values are calculated at 1 sun; 1000 data points, representing 1000 simulations, are shown in each plot. FFs are calculated from simulated J-V curves in gpvdm, using the same sets of input parameters.

10^{-1} cm^2 V^{-1} s^{-1} and 10^{-20} to 10^{-8} m^{-3} s^{-1}, respectively. In the case of trap-mediated recombination, the effective trap density and characteristic energy are varied ($U_t^{\mathrm{exp}} = 10^{15} - 10^{28}$ m^{-3} eV^{-1} and $E_t = 0.05 - 0.15$ eV). The results for $\Gamma_{m,\mathrm{dir}}$ calculated using Eq. (10) and $\Gamma_{m,t}$ using Eq. (23) are compared to FFs obtained from J-V curves calculated using gpvdm [32,33,61] in Fig. 2. We note that gpvdm has been validated against experimental data in the past [33,62,63]. Despite that, for extreme low values of $\Gamma_{m,\mathrm{dir}}$, FF goes down with $\Gamma_{m,\mathrm{dir}}$, within commonly observed FF values in the range from 50% to 70%, we find that FF increases with Γ_m for both direct and

trap-mediated recombination. This is a similar trend to that first observed by Koster and co-workers [29]. This agreement supports the validity of our analytical model under 1 sun illumination.

B. Comparison of the analytical and numerical models over a range of light intensities

1. Direct recombination

Figure 3(a) shows the correlation between $\Gamma_{m,\mathrm{dir}}$ and light intensity (without any traps) based on the analytical model, Eq. (10), with $w = 0.8$. Figures S4 and S6 within
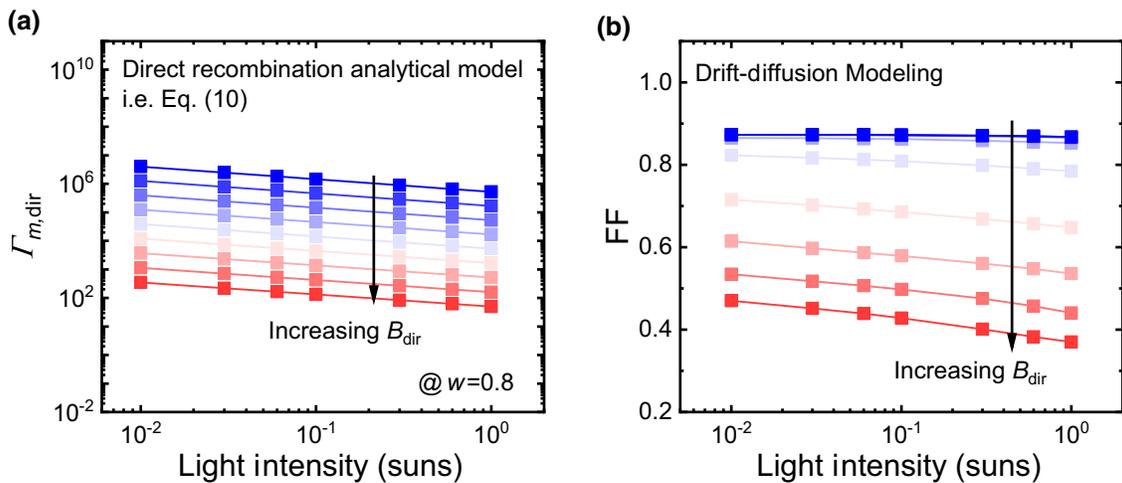
FIG. 3.   Direct recombination: comparison between (a) $\Gamma_{m,\mathrm{dir}}$ and light intensity using Eq. (10) with $w = 0.8$, and (b) numerically calculated FF versus light intensity from one-dimensional drift-diffusion simulations using gpvdm. B_{dir} was varied from 10^{-19} to 10^{-11} m^{-3} s^{-1}.

the Supplemental Material [52] show that different values of w produce similar trends and do not affect the main conclusions made in the analysis. $\Gamma_{m,\text{dir}}$ always shows negative dependence on the light intensity over a wide range of values of B_{dir}. The slope of the traces also remains constant, indicating that, for devices dominated by direct recombination, FF is expected to decrease with increasing light intensity. This result could explain the commonly observed FF-I relation in the literature. The input parameters are shown in Table S2 within the Supplemental Material [52]. Notably, this analytical model relies on low-mobility semiconductors. In the case of a crystalline silicon solar cell, transport is fast, so the FF increases with increasing light intensity based on diode-equation analysis [40]. We also find that, in our drift-diffusion simulations, high-mobility devices follow the ideal diode equations, while low-mobility devices follow our analytical model, as shown in Fig. S2 within the Supplemental Material [52]. A simple way to understand the effect of low mobility is to introduce a high transport (series) resistance in a diode model, and more discussion can be found in Sec. VI within the Supplemental Material [52]. Therefore, the commonly observed negative FF-I relation in organic solar cells can be explained by the low-mobility-induced transport resistance. While our analytical model cannot explain devices with ideal transport, it is useful for understanding devices based on low-mobility materials ($\mu < 10^{-1}$ cm^2 V^{-1} s^{-1}).

The analytical results are also compared to FF values extracted from one-dimensional drift-diffusion simulations of J-V curves over a range of light intensities and direct recombination coefficients (10^{-19}–10^{-11} m^{-3} s^{-1}) using the same base parameter set (Table S3 within the Supplemental Material [52]) in gpvdm [32,33,61] [see Fig. 3(b)]. The simulations confirm that FF decreases with increasing light intensity, regardless of the value of B_{dir}. For low values of B_{dir} ($<10^{-17}$ m^{-3} s^{-1}), the slope of the FF versus light intensity curve is shallow and the value of FF tends to its upper limit, as described by the Shockley-Queisser theory [64]. While the analytical model cannot reproduce this low B_{dir} limit, the agreement in trend between the analytical model and the drift-diffusion simulation results is good, at least for nonideal solar cells with moderate recombination coefficients.

2. Tail-state-mediated recombination

The effect of tail states on the $\Gamma_{m,t}$ versus I relation calculated using Eq. (23) is shown in Figs. 4(a)–4(f). We vary two key variables for the calculations: the characteristic energy, E_t, and the effective density of trap states, U_t^{exp}. The characteristic energy is reported to vary from 0.03 to 0.08 eV [65–68]. Here, we compare low (0.03 eV), moderate (0.06 eV), and high (0.10 eV) characteristic energies with different effective tail-state densities.

Figures 4(a)–4(c) show that E_t changes the mobility (μ_{eff})-light intensity (I) dependence significantly. With a low characteristic energy ($E_t = 0.03$ eV), μ_{eff} is largely unaffected by I, even with reasonably high effective trap densities (10^{24} m^{-3} eV^{-1}). By contrast, for larger characteristic energies, $E_t > 2k_BT$ ($E_t = 0.06$ or 0.10 eV), μ_{eff} is clearly reduced with increasing U_t^{exp} and lower light intensity. Consequently, as described by Eq. (23), the $\Gamma_{m,t}$ versus I relation is strongly affected by μ_{eff}. With low values of E_t, $\Gamma_{m,t}$ always shows a negative dependence on light intensity, and the value of U_t^{exp} has little effect on the curve. With a high value of E_t, a clear change in the $\Gamma_{m,t}$ versus I gradient with different values of U_t^{exp} is observed: the higher the value of U_t^{exp}, the more positive the slope of the $\Gamma_{m,t}$ versus I curve. These results clearly demonstrate that charge transport and recombination involving tail states can have a strong influence on the shape of the FF-I plot. The observed trend is attributable to the reduced effective charge-transport mobility when trapping and detrapping process are involved. The input parameters used in the analytical model are listed in Table I.

We also perform one-dimensional drift-diffusion simulations with an exponential distribution of trap states using gpvdm [32,33,61], and the FFs are calculated at different light intensities. A comparison of the results based on the same parameters as those given in Table S3 within the Supplemental Material [52] are shown in Figs. 4(g)–4(l). Figure S7 within the Supplemental Material [52] shows the effect of capture cross sections on the FF-I relation. Values of the cross section for capture of free to trapped electrons (holes) are chosen to ensure a fast charge-capture (trapping) rate, and hence, traps are active. The capture cross section of the conduction-band tail is chosen to be at least three orders of magnitude higher for the capture of electrons (trapping) relative to the capture cross sections for holes (recombination). For the valence-band tail, this ratio is inverted, with hole capture being more efficient than that of electron capture. Thereby, the conduction- (valence-) band tail is heavily populated with trapped electrons (holes), without the recombination rate being overwhelmingly high. The capture cross sections of holes (electrons) in the conduction- (valence-) band tail are, however, still high enough to ensure that recombination occurs primarily via tail states. The high ratio between trapping and recombination cross sections ensures that charge density is able to build up in the tail before recombining, leading to light-intensity-dependent effects, such as the light-intensity-dependent mobility that is often seen in organic semiconductors [46,47].

With a low value of E_t (30 meV), μ_{eff} at the MPP does not show a notable variation with light intensity [Fig. 4(g)]. Simultaneously, the FF shows a continuous increase with reduced light intensity, with a shallow gradient due to negligible recombination [Fig. 4(j)]. In this instance, the effect of traps density is negligible, providing
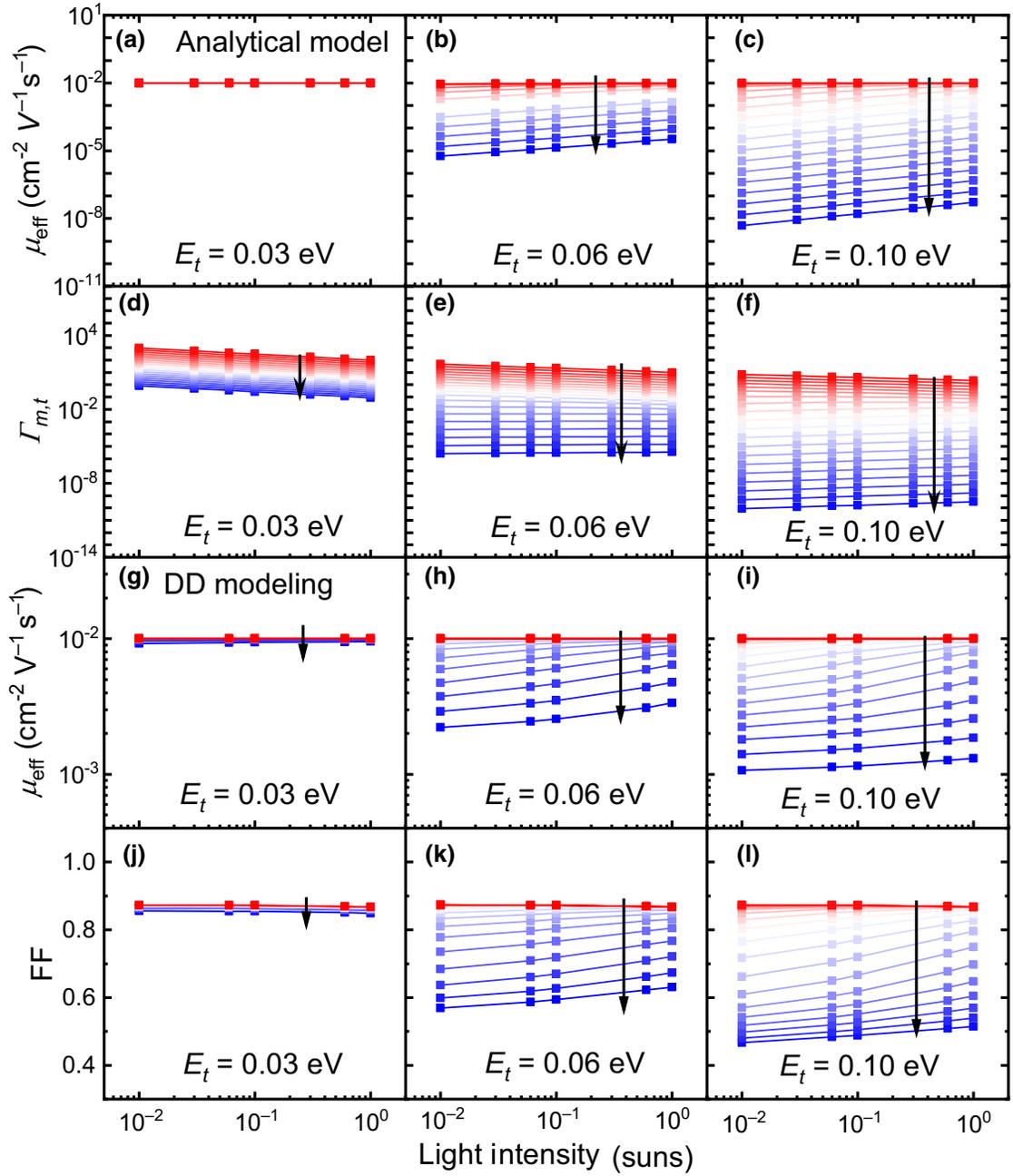
FIG. 4. Tail-state-mediated recombination: analytical model Eq. (23) ($w = 0.8$) compared with numerical drift-diffusion (DD) simulation results. (a)–(c) Carrier mobility and (d)–(f) $\Gamma_{m,t}$ as a function of light intensity, with respect to different effective trap densities for (a),(d) low (0.03 eV), (b),(e) moderate (0.06 eV), and (c),(f) high (0.10 eV) exponential characteristic energy (E_t) using analytical model Eq. (23). Drift-diffusion simulation (gpvdm) results: (g)–(i) μ_{eff} at MPP and (j)–(l) FF as a function of light intensity for (g),(j) low, (h),(k) moderate, and (i),(l) high characteristic energy. Effective density of tail states, U_t^{exp}, is varied from 10^{18} to 10^{24} m^{-3} eV^{-1}, as shown from red to blue lines.

the effective trap density (U_t^{exp}) is less than 10^{24} m^{-3} eV^{-1}. With higher values of E_t (0.06 or 0.10 eV), but low U_t^{exp} (10^{18} m^{-3} eV^{-1}), μ_{eff} at the MPP remains unchanged with varied light intensity [Figs. 4(h) and 4(i)], and FF shows a similar trend to the $E_t = 30$ meV case [Figs. 4(k) and 4(l)]. However, when U_t^{exp} is increased, μ_{eff} at the

MPP starts to decrease notably with reduced light intensity [Figs. 4(h) and 4(i)], and the slope of FF-I plot switches from negative to positive with light intensity [Figs. 4(k) and 4(l)]. The decrease of μ_{eff} at the MPP for devices with high E_t and U_t^{exp} is caused by the reduced free-to-total charge-carrier ratio ($[n_f / (n_t + n_f)]$) at low light intensity

TABLE I.   Key input parameters for analytical model Eq. (23).[a]

Parameters	Symbol	Values	Units
Temperature	T	300	K
Effective density of states of free charges	N_C, N_V	1×10^{25}	m^{-3}
Active layer thickness	L	100	nm
Effective electron trap density per unit energy	U_t^{exp}	Varied	m^{-3} eV^{-1}
Exponential tail-state DOS characteristic energy	E_t	Varied	eV
Trap-free mobility	μ_0	1×10^{-2}	cm^2 V^{-1} s^{-1}
Built-in voltage	V_{BI}	1.6	V
Trap-mediated recombination coefficient	B_t	1×10^{-8}	m^3 s^{-1}
Generation rate at 1 sun	C_G	2×10^{28}	m^{-3} s^{-1}

[a] V_{BI} follows effective band gap E_g, since we consider ideal Ohmic contact with no contact barriers. The choice of E_g or V_{BI} is made based on recent development for nonfullerene acceptors [83–87], which often present an E_g of 1.6 eV. We also note here that the FF-*I* relation is maintained, regardless of the value of V_{BI} (see Fig. S10 within the Supplemental Material [52]).

relative to 1 sun. Recall from Eq. (12) that we expect the carrier densities to depend on quasi-Fermi-level splitting, such as $n_t \propto \exp[-(\Delta E_F/E_t)]$ and $n_f \propto \exp[-(\Delta E_F/k_B T)]$. At low light intensities below 1 sun, n_t is much higher than n_f, owing to the difference in the exponential terms when N_t is large and $E_t > k_B T$. In this situation, $n_f/(n_t + n_f)$ is very small. With increased light intensity, n_f increases at a faster rate than that of n_t, and at 1 sun this makes the ratio $n_f/(n_t + n_f)$ much larger than that at lower light intensities.

The effects of the effective mobility (μ_{eff}) on the FF-*I* relation can also be explained in terms of the relative recombination rate. Inefficient charge transport will result in a higher recombination rate at a given light intensity and voltage. It follows that, at low light intensity, the recombination rate relative to the generation rate at voltages less than V_{OC}, $[R(V)/G]$, is expected to be higher than that under 1 sun illumination. Figure 5 shows calculated $R(V)/G$ as a function of voltage for two devices that have

different U_t^{exp} (10^{18} and 10^{22} m^{-3} eV^{-1}), but the same E_t (100 meV), using gpvdm. The devices show positive and negative FF-*I* relations for high and low U_t^{exp}, respectively, as shown in Fig. 4(l). With low U_t^{exp} [Fig. 5(a)], $R(V)/G$ at V_m is lower at low light intensity (0.01 sun) relative to 1 sun, indicating lower recombination, consistent with higher FF. However, with high U_t^{exp} [Fig. 5(b)], at 0.01 sun, $R(V)/G$ is significantly higher than that at 1 sun across the range of scanned voltages, which suggests higher recombination rates and lower FF at $I = 0.01$ sun. The analysis in terms of relative recombination rate is consistent with that based on the effective mobility.

These results based on numerical simulations using gpvdm are consistent with the observations from our analytical model. We also rule out the possibility that interfacial contact barriers at the electrodes cab produce a positive FF-*I* dependence (see Sec. X within Supplemental Material for further details [52]). We conclude that the influence of tail states can theoretically account for
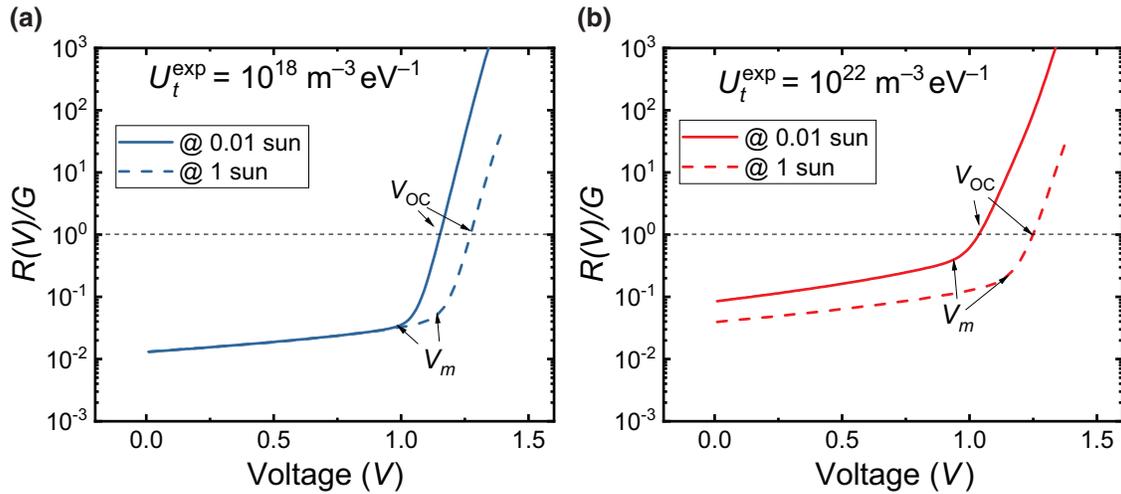
FIG. 5.   Calculated relative recombination rate [$R(V)/G$] using gpvdm as a function of voltage for devices with (a) low (10^{18} m^{-3} eV^{-1}) and (b) high (10^{22} m^{-3} eV^{-1}) effective trap density (U_t^{exp}). E_t is set to be 100 meV.

different FF-*I* relationships. These results combined with those in Fig. 3 also show that our analytical models can be useful for both 1 sun and light-intensity-dependent analysis of FFs.

IV. EXPERIMENTAL RESULTS

Having investigated the relationship between FF and light intensity theoretically, we now proceed to demonstrate the modeled FF-*I* behavior using practical organic-solar-cell devices.

A. Experimental FF-*I* relation

To investigate the FF-*I* relation of practical organic-material-based solar cells, inverted architecture [Fig. 6(a)] OSCs based on PTB7-Th [34] as the donor blended with either the fullerene acceptor $PC_{71}BM$ or the nonfullerene acceptor O-IDTBR [35] are fabricated (see the Experimental Section within the Supplemental Material [52] for more details regarding device fabrication). The energy-level alignment of the studied materials [35,69–75] and contacts [76] is presented in Fig. S11 within the Supplemental Material [52]. Current density-voltage (*J-V*) curves

for PTB7-Th:$PC_{71}BM$ and PTB7-Th:O-IDTBR devices under AM1.5 G simulated sunlight at different illumination intensities are measured, with the resulting FF-*I* data shown in Fig. 6(b). Devices based on $PC_{71}BM$ and O-IDTBR show completely different responses to the irradiation intensity under a simulated AM 1.5 G solar spectrum in terms of FF. For PTB7-Th:O-IDTBR devices, the FF increases with illumination intensity, while the FF of the PTB7-Th:$PC_{71}BM$ device has a negative dependence on the irradiation intensity, as previously seen in the literature [16–21].

As the effect of leakage current has often been used to explain the FF reduction at low light intensity [15,23], we first compare the dark current density with the light current density at different illumination intensities, as shown in Figs. 6(c) and 6(d). Although the reverse dark current of the $PC_{71}BM$-based device is around one order of magnitude lower than that of the O-IDTBR device, we find that the dark current for both devices is greater than one order of magnitude lower than the current density under the lowest light intensity ($3\,mW\,cm^{-2}$). In addition, the reduction of FF for O-IDTBR devices becomes apparent at 1 sun, where the current density is at least two orders of
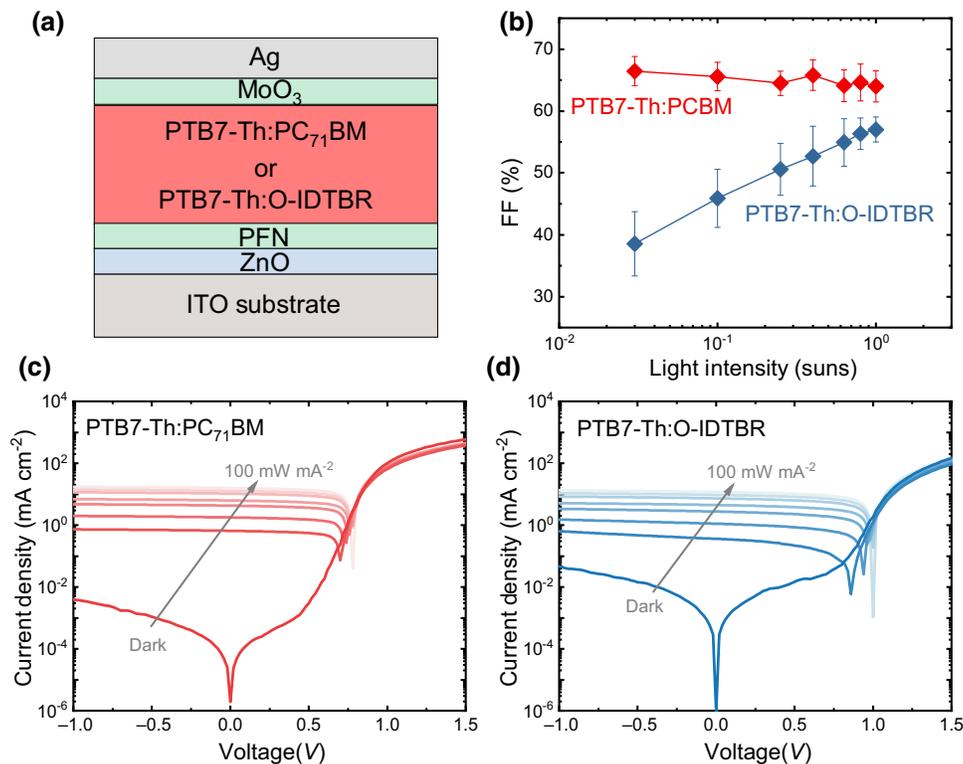
FIG. 6. Device structure, experimental FF-*I* results, and current density-voltage characteristics. (a) Inverted device structure for the organic-solar-cell fabrication: ITO/ZnO/PFN/PTB7-Th:$PC_{71}BM$ (1:1.5 ratio by mass, 80 ± 5 nm) or PTB7-Th:O-IDTBR (1:1 ratio by mass, 80 ± 5 nm)/MoO_3/Ag. (b) Averaged fill factor with standard derivations as a function of light intensity, as extracted from current density-voltage characteristics. At least three devices are measured for both the PTB7-Th:$PC_{71}BM$ and PTB7-Th:O-IDTBR architectures. Current density-voltage curves at different light intensities for (c) PTB7-Th:$PC_{71}BM$ and (d) PTB7-Th:O-IDTBR devices. A single representative device of each type is shown.

magnitude higher than the dark current density, suggesting the origin is unlikely to be the leakage current, in this case. However, the fact that the O-IDTBR device presents a higher reverse dark current than that of the $PC_{71}BM$ device is an indication that the O-IDTBR device suffers more recombination than that of the $PC_{71}BM$ device. The two devices provide contrasting examples to understand the factors that control the FF-*I* relation in organic disordered-semiconductor-based solar cells.

B. Quantifying trap states

We show that both the analytical and numerical (drift-diffusion) modeling results indicate that direct recombination cannot produce a positive dependence of FF on light intensity in low-mobility semiconductor-based solar cells. Conversely, the existence of a significant density of exponential-type trap states can affect the FF-*I* relation in such a way that FF is reduced at lower light intensities. In this section, we show that the different FF-*I* dependencies of the two devices studied can be directly related to their different trap state densities.

1. Ideality factors

Measurements of device ideality factors have frequently been used to indicate the degree of recombination via trap states in OSCs [56]. As derived in Eq. (17), higher ideality factors correspond to a greater proportion of recombination via trap states.

We extract the ideality factor ($n_{id,l}$) of the measured devices using the V_{OC} versus light intensity plot (suns-V_{OC}), as shown in Fig. 7. The ideality factors calculated from the slope of the curve fits are 1.00 ± 0.10 and 1.60 ± 0.20 for the $PC_{71}BM$ and O-IDTBR devices,
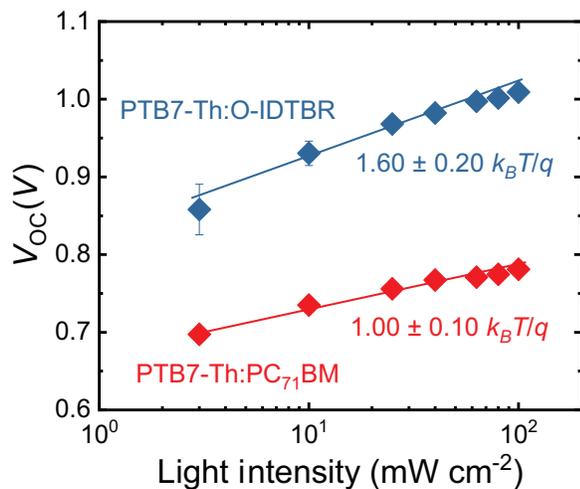
FIG. 7. Experimental measured ideality factors. Open-circuit voltage (V_{OC}) versus light intensity (I). Solid lines are fits to the data indicated by diamond markers.

respectively. We also estimate the dark ideality factor, $n_{id,d}$, using dark *J-V* curves, showing the same trend as that of $n_{id,l}$ (see the Methods section and Fig. S12 within the Supplemental Material for further details [52]).

The O-IDTBR device presents notably higher ideality factors (closer to 2) than those of the $PC_{71}BM$ device (close to 1), indicating that trap-mediated recombination is likely to play a bigger role in the O-IDTBR devices than that in the $PC_{71}BM$ devices.

2. Low-frequency capacitance

Ideality factor measurements indicate that the O-IDTBR device likely presents more trap-mediated recombination than that of the $PC_{71}BM$ device. In this section, we directly measure the trap state density of devices using low-frequency (10 kHz) capacitance measurements [51, 77–79]. Since the measurement frequency approaches the timescale of trapping and detrapping, trapped carriers can respond to the alternating internal electric field. It has previously been argued that an increase in capacitance at higher applied dc voltages can be attributed to trap states mediating the charge distribution and transport [51,77–79], suggesting that an extended density of trap states is the origin of the low-frequency capacitance enhancement.

We adapt this concept to understand the influence of illumination intensity on the low-frequency capacitance within the multiple trapping and detrapping model. In the low-frequency regime studied, the effects of deep traps cannot be detected, while shallow traps can be. Under low illumination, the trap states are not fully occupied and carriers mostly fill the deep states. As such, the detrapping rate is low, owing to its exponential dependence on trap depth (E_{depth}), via $\propto \exp[-(E_{depth}/k_B T)]$. Deeply trapped carriers, therefore, do not strongly influence carrier dynamics. With increased light intensity, however, the shallow states start to be filled. In this situation, the rate of detrapping becomes significant, such as to influence transport, and results in an increase in the measured capacitance [77]. Hence, the enhancement of capacitance at high light intensity is an indication of trap-mediated charge dynamics. The effect of trapping is expected to be more pronounced with a low internal field, where charge extraction is slow. Measuring the capacitance response at low frequency under a range of applied voltages is therefore a useful method to detect the shallow trap states.

Here, we apply these concepts to our OPV devices and perform capacitance-voltage (*C-V*) measurements under 10 kHz frequency at different applied dc voltages, starting from −2 to 2 V. Figure 8(a) shows the capacitance measured using a 50 mV ac voltage set at 10 kHz for the $PC_{71}BM$- and O-IDTBR-based devices measured at various light intensities (from 1 sun to the dark). On applying a negative bias of −2 V, the capacitance converges to the geometric capacitance. In this regime, the
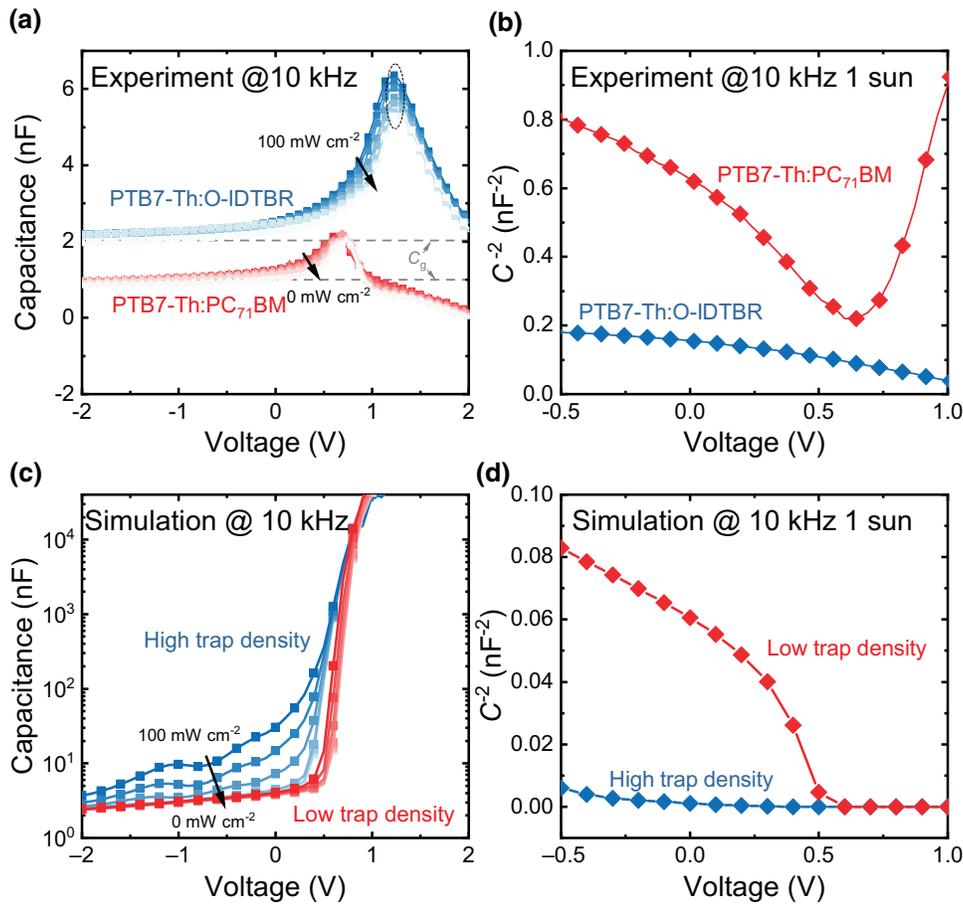
FIG. 8. Experimentally measured and simulated capacitance versus voltage characteristics. Experimental (a) C versus V characteristics at various light intensities and (b) $1/C^2$ versus V characteristics at 1 sun illumination under 10 kHz alternating voltage for PTB7-Th:PC$_{71}$BM and PTB7-Th:O-IDTBR solar cells. Calculated (c) C - V characteristics at different light intensities and (d) $1/C^2$ versus V characteristics at 1 sun illumination under 10 kHz alternating voltage for simulated devices with low (10^{18} m^{-3} eV^{-1}) and high (10^{24} m^{-3} eV^{-1}) effective trap densities with the same characteristic energy for traps ($E_t = 0.10$ eV).

strong electric field under large negative applied bias efficiently removes carriers, such that charge recombination, transport, or redistribution caused by trapping and detrapping are small and hardly interfere with the dynamics of charge carriers. With increased voltage, the electrostatic potential difference between the contacts drops, leading to reduced drift currents. From this point, trap states start to play an active role in mediating charge-carrier transport processes, resulting in the increased capacitance seen in Fig. 8(a). Both PC$_{71}$BM and O-IDTBR devices present an increased capacitance with reduced internal field, indicating that trap-mediated transport exists in both devices. However, a clear magnitude of difference between the O-IDTBR and PC$_{71}$BM devices is observed. The capacitance at low internal field (corresponding to ∼1.2 V voltage) caused by trapping and detrapping of carriers shows a large enhancement, relative to the capacitance at the high internal field at high light intensity, while the enhancement is lower for lower light intensities due to the deep depth of filled trap states in the case of the O-IDTBR

devices. For the PC$_{71}$BM devices, at low and high light intensity, the magnitude of capacitance enhancement from negative to positive voltage is similar to, but significantly smaller than, that for O-IDTBR devices. This suggests that there are significantly more occupied trap states in the O-IDTBR device than those in the PC$_{71}$BM devices.

According to Ref. [77], under low frequency and high light intensities, the capacitance caused by trapping and detrapping processes gives information about the lower limit of the trap density corresponding to shallow traps. Here, deeper trap states can be probed only at low frequency on the same order as that of their detrapping rates. Assuming the additional capacitance at V close to V_{BI} is caused by trapped carriers being released to the mobility edges, the trapped charge density of accessible trap states can be estimated by [77,80,81]

$$\frac{1}{C^2} \propto -\frac{2}{N_t \varepsilon q A^2} V, \tag{24}$$

where ε is the dielectric constant, C is the capacitance, A is the device area, and V is the applied voltage.

We obtain the trap density by fitting $1/C^2$ versus V plots at 1 sun over the voltage range close to V_{BI}, as shown in Fig. 8(b). The slope of $1/C^2$ versus V in the PC$_{71}$BM device is significantly higher than that of the O-IDTBR device (comparing positive values), indicating that the trap density is much lower in the PC$_{71}$BM device than that in the O-IDTBR device. Using Eq. (24), we obtain values of 2.5×10^{22}, and 2.0×10^{23} m^{-3} for the PC$_{71}$BM and O-IDTBR devices at 10 kHz, respectively. The exact values of the total trap density in the two devices are difficult to determine, since it is hard to obtain clean signals at extremely low frequencies due to experimental system noise, and the trap densities estimated above can be related only to the accessible traps at 10 kHz frequency and under 1 sun illumination. However, the higher trap density extracted from the capacitance-voltage analysis is strong evidence that the O-IDTBR device has a higher total trap state density than that of the PC$_{71}$BM device.

To verify our conclusions from the capacitance measurement, we perform C-V simulations at 10 kHz with a 50 mV ac voltage under different light intensities (the same as experimental C-V measurements) using gpvdm [32]. These C-V simulations are fully time resolved and no additional assumptions are made, such as linearization of the equations. Since we do not know the precise parameters, e.g., trap profile and density in the real devices, we do not perform a fitting routine on the experimental C-V curves, but rather aim for qualitative agreement. The simulations are carried out at $E_t = 0.10$ eV with the same parameter set as that listed in Table S3 within the Supplemental Material [52]. The built-in voltage is set to 1 V and the zero-field mobility is set to 1×10^{-3} cm^2 V^{-1} s^{-1}. We compare low (10^{18} m^{-3} eV^{-1}) and high (10^{24} m^{-3} eV^{-1}) effective trap densities. As shown in Fig. 8(c), although the magnitude of calculated C-V characteristics are much higher than that of the measured C-V, the simulated device with high trap density shows a much larger capacitance enhancement than that of the device with low trap density, when we increase the light intensity from dark to 1 sun. This result is consistent with prior theory [77], namely, that traps have a strong influence on the capacitance signal under a low-frequency ac voltage. We also calculate $1/C^2$ versus V characteristics at 1 sun, as shown in Fig. 8(d). A clear slope difference is observed between low- and high-trap-density devices, which is also qualitatively consistent with the experimental results. Good agreement between experiments and simulations strongly supports our conclusions that the O-IDTBR device has a higher trap state density than that of the PC$_{71}$BM device.

In summary, the O-IDTBR device presents a higher ideality factor, stronger trapping and detrapping behavior, and higher trap density than those of the PC$_{71}$BM device. Consistent with our analytical model, the reduction of FF at low light intensity can be correlated to the existence of a significant density of tail states mediating carrier transport.

V. CONCLUSIONS

We propose an analytical model parameterized by the transport-to-recombination factor, Γ_m, to help to understand the correlation between fill factor and light intensity in organic disordered-semiconductor-based solar cells. The analytical model suggests that, for low-mobility devices limited by direct recombination, $\Gamma_{m,\text{dir}}$ always decreases with light intensity due to low-mobility-induced transport resistance. This accounts for the observed FF-I relation, where FF depends negatively on light intensity. For tail-state-mediated transport and recombination, a positive dependence of $\Gamma_{m,t}$ on light intensity can be derived in cases where the characteristic energy (E_t) is greater than $2k_BT$ (52 meV at room temperature), resulting in a positive dependence of fill factor on light intensity. Charge-density-dependent carrier mobility caused by carrier trapping and detrapping and a low reaction order are the principal origins of the positive FF-I relation. Our analytical models are verified using numerical drift-diffusion simulations (gpvdm) for both 1 sun and light-intensity-dependent analyses.

To further verify the proposed analytical model, we characterize PTB7-Th:PC$_{71}$BM and PTB7-Th:O-IDTBR organic solar cells that show negative and positive FF-I relations, respectively. Detailed experimental investigation shows that the O-IDTBR device has a higher ideality factor, stronger carrier trapping and detrapping behavior, and a higher density of trap states than those of the PC$_{71}$BM device. These experimental findings are consistent with the results from our analytical and numerical models, indicating the importance of tail states in the analysis of light-intensity dependence of fill factor in disordered-semiconductor-based solar cells.

The findings herein are particularly significant for devices that target low- or high-light-intensity applications, such as indoor and concentrated photovoltaics. The conclusions can be extended from organic semiconductors to other disordered-absorber materials. The analytical model provides a physical understanding of the relationship between fill factor and light intensity and the role played by tail states in this relation. It follows that measuring FF-I is a powerful technique to further characterize the density and nature of tail states in disordered-semiconductor-based solar-cell devices.

———————————

[1] G. Li, R. Zhu, and Y. Yang, Polymer solar cells, Nat. Photonics **6**, 153 (2012).

[2] R. A. J. Janssen and J. Nelson, Factors limiting device efficiency in organic photovoltaics, Adv. Mater. **25**, 1847 (2013).

[3] J. Nelson, Polymer: Fullerene bulk heterojunction solar cells, Mater. Today **14**, 462 (2011).

[4] A. J. Heeger, 25th anniversary article: Bulk heterojunction solar cells: Understanding the mechanism of operation, Adv. Mater. **26**, 10 (2014).

[5] J. Hou, O. Inganäs, R. H. Friend, and F. Gao, Organic solar cells based on non-fullerene acceptors, Nat. Mater. **17**, 119 (2018).

[6] J. Nelson, J. J. Kwiatkowski, J. Kirkpatrick, and J. M. Frost, Modeling charge transport in organic photovoltaic materials, Acc. Chem. Res. **42**, 1768 (2009).

[7] J. Nelson, *The Physics of Solar Cells, The Physics of Solar Cells* (Imperial College Press, London, 2003).

[8] H. K. H. Lee, J. Wu, J. Barbé, S. M. Jain, S. Wood, E. M. Speller, Z. Li, F. A. Castro, J. R. Durrant, and W. C. Tsoi, Organic photovoltaic cells – promising indoor light harvesters for self-sustainable electronics, J. Mater. Chem. A **6**, 5618 (2018).

[9] Y. Cui, Y. Wang, J. Bergqvist, H. Yao, Y. Xu, B. Gao, C. Yang, S. Zhang, O. Inganäs, F. Gao, and J. Hou, Wide-gap non-fullerene acceptor enabling high-performance organic photovoltaic cells for indoor applications, Nat. Energy **4**, 768 (2019).

[10] S. R. Cowan, A. Roy, and A. J. Heeger, Recombination in polymer-fullerene bulk heterojunction solar cells, Phys. Rev. B - Condens. Matter Mater. Phys. **82**, 1 (2010).

[11] L. J. A. Koster, V. D. Mihailetchi, H. Xie, and P. W. M. Blom, Origin of the light intensity dependence of the short-circuit current of polymer/fullerene solar cells, Appl. Phys. Lett. **87**, 203502 (2005).

[12] A. K. K. Kyaw, D. H. Wang, V. Gupta, W. L. Leong, L. Ke, G. C. Bazan, and A. J. Heeger, Intensity dependence of current–voltage characteristics and recombination in high-efficiency solution-processed small-molecule solar cells, ACS Nano **7**, 4569 (2013).

[13] L. J. A. Koster, V. D. Mihailetchi, R. Ramaker, and P. W. M. Blom, Light intensity dependence of open-circuit voltage of polymer:Fullerene solar cells, Appl. Phys. Lett. **86**, 123509 (2005).

[14] A. Maurano, C. G. Shuttle, R. Hamilton, A. M. Ballantyne, J. Nelson, W. Zhang, M. Heeney, and J. R. Durrant, Transient optoelectronic analysis of charge carrier losses in a selenophene/fullerene blend solar cell, J. Phys. Chem. C **115**, 5947 (2011).

[15] C. M. Proctor and T.-Q. Nguyen, Effect of leakage current and shunt resistance on the light intensity dependence of organic solar cells, Appl. Phys. Lett. **106**, 083301 (2015).

[16] C. M. Proctor, C. Kim, D. Neher, and T.-Q. Nguyen, Nongeminate recombination and charge transport limitations in diketopyrrolopyrrole-based solution-processed small molecule solar cells, Adv. Funct. Mater. **23**, 3584 (2013).

[17] L. H. Slooff, S. C. Veenstra, J. M. Kroon, W. Verhees, L. J. A. Koster, and Y. Galagan, Describing the light intensity dependence of polymer:Fullerene solar cells using an adapted shockley diode model, Phys. Chem. Chem. Phys. **16**, 5732 (2014).

[18] J. You, L. Dou, K. Yoshimura, T. Kato, K. Ohya, T. Moriarty, K. Emery, C.-C. Chen, J. Gao, G. Li, and Y. Yang, A polymer tandem solar cell with 10.6% power conversion efficiency, Nat. Commun. **4**, 1446 (2013).

[19] Y. Galagan, A. Manor, R. Andriessen, and E. A. Katz, in 2012 38th IEEE Photovolt. Spec. Conf. (2012), pp. 002750–002752.

[20] A. Sharma, M. Chauhan, V. Bharti, M. Kumar, S. Chand, B. Tripathi, and J. P. Tiwari, Revealing the correlation between charge carrier recombination and extraction in an organic solar cell under varying illumination intensity, Phys. Chem. Chem. Phys. **19**, 26169 (2017).

[21] C. G. Shuttle, R. Hamilton, B. C. O'Regan, J. Nelson, and J. R. Durrant, Charge-density-based analysis of the current-voltage response of polythiophene/fullerene photovoltaic devices, Proc. Natl. Acad. Sci. **107**, 16448 (2010).

[22] Y. Zhang, X.-D. Dang, C. Kim, and T.-Q. Nguyen, Effect of charge recombination on the fill factor of small molecule bulk heterojunction solar cells, Adv. Energy Mater. **1**, 610 (2011).

[23] Y. Zhou, T. M. Khan, J. W. Shim, A. Dindar, C. Fuentes-Hernandez, and B. Kippelen, All-plastic solar cells with a high photovoltaic dynamic range, J. Mater. Chem. A **2**, 3492 (2014).

[24] M. Stößel, J. Staudigel, F. Steuber, J. Blässing, J. Simmerer, and A. Winnacker, Space-charge-limited electron currents in 8-hydroxyquinoline aluminum, Appl. Phys. Lett. **76**, 115 (2000).

[25] P. E. Burrows, Z. Shen, V. Bulovic, D. M. McCarty, S. R. Forrest, J. A. Cronin, and M. E. Thompson, Relationship between electroluminescence and current transport in organic heterojunction light-emitting devices, J. Appl. Phys. **79**, 7991 (1996).

[26] R. S. Crandall, Modeling of thin film solar cells: Uniform field approximation, J. Appl. Phys. **54**, 7176 (1983).

[27] R. S. Crandall, Transport in hydrogenated amorphous silicon p - i - n solar cells, J. Appl. Phys. **53**, 3350 (1982).

[28] K. Hecht, The mechanism of the primary photoelectric current in insulating crystals, Z. Phys. **77**, 235 (1932).

[29] D. Bartesaghi, I. C. del Pérez, J. Kniepert, S. Roland, M. Turbiez, D. Neher, and L. J. A. Koster, Competition between recombination and extraction of free charges determines the fill factor of organic solar cells, Nat. Commun. **6**, 7083 (2015).

[30] M. Stolterfoht, A. Armin, B. Philippa, and D. Neher, The role of space charge effects on the competition between recombination and extraction in solar cells with Low-mobility photoactive layers, J. Phys. Chem. Lett. **7,** 4716 (2016).

[31] P. Kaienburg, U. Rau, and T. Kirchartz, Extracting Information About the Electronic Quality of Organic Solar-Cell Absorbers From Fill Factor and Thickness, Phys. Rev. Appl. **6,** 1 (2016).

[32] R. C. I. MacKenzie, General-purpose Photovoltaic Device Model—gpvdm, Https://Www.Gpvdm.Com. (n.d.).

[33] R. C. I. MacKenzie, C. G. Shuttle, M. L. Chabinyc, and J. Nelson, Extracting microscopic device parameters from transient photocurrent measurements of P3HT:PCBM solar cells, Adv. Energy Mater. **2,** 662 (2012).

[34] Z. He, B. Xiao, F. Liu, H. Wu, Y. Yang, S. Xiao, C. Wang, T. P. Russell, and Y. Cao, Single-junction polymer solar cells with high efficiency and photovoltage, Nat. Photonics **9,** 174 (2015).

[35] D. Baran, R. S. Ashraf, D. A. Hanifi, M. Abdelsamie, N. Gasparini, J. A. Röhr, S. Holliday, A. Wadsworth, S. Lockett, M. Neophytou, C. J. M. Emmott, J. Nelson, C. J. Brabec, A. Amassian, A. Salleo, T. Kirchartz, J. R. Durrant, and I. McCulloch, Reducing the efficiency-stability-cost gap of organic photovoltaics with highly efficient and stable small molecule acceptor ternary solar cells, Nat. Mater. **16,** 363 (2017).

[36] A. Wadsworth, *et al.*, Progress in poly (3-hexylthiophene) organic solar cells and the influence of Its molecular weight on device performance, Adv. Energy Mater. 8, 1 (2018).

[37] M. A. Green, Solar cell fill factors: General graph and empirical expressions, Solid. State. Electron. **24,** 788 (1981).

[38] C. van Berkel, M. J. Powell, A. R. Franklin, and I. D. French, Quality factor in a -Si:H nip and pin diodes, J. Appl. Phys. **73,** 5264 (1993).

[39] T. Kirchartz and J. Nelson, Meaning of reaction orders in polymer:Fullerene solar cells, Phys. Rev. B **86,** 165201 (2012).

[40] K. Ruhle, M. K. Juhl, M. D. Abbott, and M. Kasemann, Evaluating crystalline silicon solar cells at Low light intensities using intensity-dependent analysis of I–V parameters, IEEE J. Photovoltaics **5,** 926 (2015).

[41] N. H. Reich, W. G. J. H. M. van Sark, E. A. Alsema, R. W. Lof, R. E. I. Schropp, W. C. Sinke, and W. C. Turkenburg, Crystalline silicon cell performance at low light intensities, Sol. Energy Mater. Sol. Cells 93, 1471 (2009).

[42] T. Kirchartz, J. Bisquert, I. Mora-Sero, and G. Garcia-Belmonte, Classification of solar cells according to mechanisms of charge separation and charge collection, Phys. Chem. Chem. Phys. **17,** 4007 (2015).

[43] S. J. Robinson, A. G. Aberle, and M. A. Green, Departures from the principle of superposition in silicon solar cells, J. Appl. Phys. **76,** 7920 (1994).

[44] T. C. M. Müller, B. E. Pieters, U. Rau, and T. Kirchartz, Analysis of the series resistance in pin -type thin-film silicon solar cells, J. Appl. Phys. **113,** 134503 (2013).

[45] D. Neher, J. Kniepert, A. Elimelech, and L. J. A. Koster, A New figure of merit for organic solar cells with transport-limited photocurrents, Sci. Rep. **6,** 1 (2016).

[46] C. G. Shuttle, R. Hamilton, J. Nelson, B. C. O'Regan, and J. R. Durrant, Measurement of charge-density dependence of carrier mobility in an organic semiconductor blend, Adv. Funct. Mater. **20,** 698 (2010).

[47] M. Bouhassoune, S. L. M. van Mensfoort, P. A. Bobbert, and R. Coehoorn, Carrier-density and field-dependent charge-carrier mobility in organic semiconductors with correlated Gaussian disorder, Org. Electron. **10,** 437 (2009).

[48] R. C. I. MacKenzie, T. Kirchartz, G. F. A. Dibb, and J. Nelson, Modeling nongeminate recombination in P3HT:PCBM solar cells, J. Phys. Chem. C **115,** 9806 (2011).

[49] T. Kirchartz, B. E. Pieters, J. Kirkpatrick, U. Rau, and J. Nelson, Recombination via tail states in polythiophene:Fullerene solar cells, Phys. Rev. B: Condens. Matter Mater. Phys **83,** 1 (2011).

[50] M. Kuik, L. J. A. Koster, G. A. H. Wetzelaer, and P. W. M. Blom, Trap-assisted Recombination in Disordered Organic Semiconductors, Phys. Rev. Lett. **107,** 1 (2011).

[51] L. Burtone, J. Fischer, K. Leo, and M. Riede, Trap states in ZnPc:C60 small-molecule organic solar cells, Phys. Rev. B **87,** 045432 (2013).

[52] See the Supplemental Material at http://link.aps.org/supplemental/10.1103/PhysRevApplied.14.024034 for experimental details, method section, derivation of key equations, as well as supporting figures and tables.

[53] P. Das, Maximum power tracking based open circuit voltage method for PV system, in *Energy Procedia* (Elsevier Ltd, 2016), pp. 2–13.

[54] J. Yao, T. Kirchartz, M. S. Vezie, M. A. Faist, W. Gong, H. Wu, J. Troughton, T. Watson, and J. Nelson, Quantifying Losses in Open-Circuit Voltage in Solution Processable Solar Cells, Phys. Rev. Appl. **4,** 1 (2015).

[55] K. Tvingstedt and C. Deibel, Temperature dependence of ideality factors in organic solar cells and the relation to radiative efficiency, Adv. Energy Mater. **6,** 1502230 (2016).

[56] T. Kirchartz, F. Deledalle, P. S. Tuladhar, J. R. Durrant, and J. Nelson, On the differences between dark and light ideality factor in polymer:Fullerene solar cells, J. Phys. Chem. Lett. **4,** 2371 (2013).

[57] T. M. Burke, S. Sweetnam, K. Vandewal, and M. D. McGehee, Beyond langevin recombination: How equilibrium between free carriers and charge transfer states determines the open-circuit voltage of organic solar cells, Adv. Energy Mater. **5,** 1500123 (2015).

[58] J. Kniepert, I. Lange, N. J. van der Kaap, L. J. A. Koster, and D. Neher, A conclusive view on charge generation, recombination, and extraction in As-prepared and annealed P3HT:PCBM blends: Combined experimental and simulation work, Adv. Energy Mater. **4,** 1301401 (2014).

[59] P. Mark and W. Helfrich, Space-charge-limited currents in organic crystals, J. Appl. Phys. **33,** 205 (1962).

[60] J. A. Anta, J. Nelson, and N. Quirke, Charge transport model for disordered materials: Application to application to sensitized TiO$_2$, Phys. Rev. B **65,** 125324 (2002).

[61] N. Majeed, M. Saladina, M. Krompiec, S. Greedy, C. Deibel, and R. C. I. MacKenzie, Using deep machine learning to understand the physical performance bottlenecks in novel thin-film solar cells, Adv. Funct. Mater. **1907259,** 1907259 (2019).

[62] H. Mäckel and R. C. I. MacKenzie, Determination of Charge-Carrier Mobility in Disordered Thin-Film Solar Cells as a Function of Current Density, Phys. Rev. Appl. **9,** 34020 (2018).

[63] X. Shi, V. Nádaždy, A. Perevedentsev, J. M. Frost, X. Wang, E. von Hauff, R. C. I. MacKenzie, and J. Nelson, Relating Chain Conformation to The Density of States and Charge Transport in Conjugated Polymers: The Role of The β-Phase in Poly(9,9-Dioctylfluorene), Phys. Rev. X **9,** 021038 (2019).

[64] W. Shockley and H. J. Queisser, Detailed balance limit of efficiency of p-n junction solar cells, J. Appl. Phys. **32,** 510 (1961).

[65] S. A. Hawks, G. Li, Y. Yang, and R. A. Street, Band tail recombination in polymer:Fullerene organic solar cells, J. Appl. Phys. **116,** 074503 (2014).

[66] R. A. Street, Localized state distribution and its effect on recombination in organic solar cells, Phys. Rev. B **84,** 075208 (2011).

[67] R. A. Street, A. Krakaris, and S. R. Cowan, Recombination through different types of localized states in organic solar cells, Adv. Funct. Mater. **22,** 4608 (2012).

[68] J. Wu, J. Luke, H. K. H. Lee, P. Shakya Tuladhar, H. Cha, S.-Y. Jang, W. C. Tsoi, M. Heeney, H. Kang, K. Lee, T. Kirchartz, J.-S. Kim, and J. R. Durrant, Tail state limited photocurrent collection of thick photoactive layers in organic solar cells, Nat. Commun. **10,** 5159 (2019).

[69] L. Zhang, T. Yang, L. Shen, Y. Fang, L. Dang, N. Zhou, X. Guo, Z. Hong, Y. Yang, H. Wu, J. Huang, and Y. Liang, Toward highly sensitive polymer photodetectors by molecular engineering, Adv. Mater. **27,** 6496 (2015).

[70] Y. Zhang, D. Deng, K. Lu, J. Zhang, B. Xia, Y. Zhao, J. Fang, and Z. Wei, Synergistic effect of polymer and small molecules for high-performance ternary organic solar cells, Adv. Mater. **27,** 1071 (2015).

[71] T. Jiang, J. Yang, Y. Tao, C. Fan, L. Xue, Z. Zhang, H. Li, Y. Li, and W. Huang, Random terpolymer with a cost-effective monomer and comparable efficiency to PTB7-Th for bulk-heterojunction polymer solar cells, Polym. Chem. **7,** 926 (2016).

[72] M.-A. Pan, T.-K. Lau, Y. Tang, Y.-C. Wu, T. Liu, K. Li, M.-C. Chen, X. Lu, W. Ma, and C. Zhan, 16.7%-efficiency ternary blended organic photovoltaic cells with PCBM as the acceptor additive to increase the open-circuit voltage and phase purity, J. Mater. Chem. A **7,** 20713 (2019).

[73] L. Hu, W. Qiao, J. Qi, X. Zhang, J. Han, and C. Wang, Significant enhancement of photodetector performance by subtle changes in the side chains of dithienopyrrole-based polymers, RSC Adv. **6,** 22494 (2016).

[74] S. Holliday, R. S. Ashraf, A. Wadsworth, D. Baran, S. A. Yousaf, C. B. Nielsen, C. H. Tan, S. D. Dimitrov, Z. Shang, N. Gasparini, M. Alamoudi, F. Laquai, C. J. Brabec, A. Salleo, J. R. Durrant, and I. McCulloch, High-efficiency and air-stable P3HT-based polymer solar cells with a new non-fullerene acceptor, Nat. Commun. **7,** 1 (2016).

[75] S.-H. Liao, H.-J. Jhuo, Y.-S. Cheng, and S.-A. Chen, Fullerene derivative-doped zinc oxide nanofilm as the cathode of inverted polymer solar cells with Low-bandgap polymer (PTB7-Th) for high performance, Adv. Mater. **25,** 4766 (2013).

[76] R. Xia, D. S. Leem, T. Kirchartz, S. Spencer, C. Murphy, Z. He, H. Wu, S. Su, Y. Cao, J. S. Kim, J. C. Demello, D. D. C. Bradley, and J. Nelson, Investigation of a conjugated polyelectrolyte interlayer for inverted polymer:Fullerene solar cells, Adv. Energy Mater. **3,** 718 (2013).

[77] D. Ray, L. Burtone, K. Leo, and M. Riede, Detection of trap charge in small molecular organic bulk heterojunction solar cells, Phys. Rev. B **82,** 125204 (2010).

[78] L. Burtone, D. Ray, K. Leo, and M. Riede, Impedance model of trap states for characterization of organic semiconductor devices, J. Appl. Phys. **111,** 064503 (2012).

[79] P. P. Boix, G. Garcia-Belmonte, U. Muñecas, M. Neophytou, C. Waldauf, and R. Pacios, Determination of gap defect states in organic bulk heterojunction solar cells from capacitance measurements, Appl. Phys. Lett. **95,** 233302 (2009).

[80] J. D. Cohen and D. V. Lang, Calculation of the dynamic response of schottky barriers with a continuous distribution of gap states, Phys. Rev. B **25,** 5321 (1982).

[81] L. C. Kimerling, Influence of deep traps on the measurement of free-carrier distributions in semiconductors by junction capacitance techniques, J. Appl. Phys. **45,** 1839 (1974).

[82] S. M. Sze and K. K, *Ng, Physics of Semiconductor Devices, Physics of Semiconductor Devices* (John Wiley & Sons, Inc, Hoboken, NJ, USA, 2006).

[83] J. Yuan, T. Huang, P. Cheng, Y. Zou, H. Zhang, J. L. Yang, S.-Y. Chang, Z. Zhang, W. Huang, R. Wang, D. Meng, F. Gao, and Y. Yang, Enabling low voltage losses and high photocurrent in fullerene-free organic photovoltaics, Nat. Commun. **10,** 570 (2019).

[84] Y. Cui, H. Yao, J. Zhang, T. Zhang, Y. Wang, L. Hong, K. Xian, B. Xu, S. Zhang, J. Peng, Z. Wei, F. Gao, and J. Hou, Over 16% efficiency organic photovoltaic cells enabled by a chlorinated acceptor with increased open-circuit voltages, Nat. Commun. **10,** 2515 (2019).

[85] C. Zhu, J. Yuan, F. Cai, L. Meng, H. Zhang, H. Chen, J. Li, B. Qiu, H. Peng, S. Chen, Y. Hu, C. Yang, F. Gao, Y. Zou, and Y. Li, Tuning the electron-deficient core of a non-fullerene acceptor to achieve over 17% efficiency in a single-junction organic solar cell, Energy Environ. Sci. (2020).

[86] J. Zhang, W. Liu, M. Zhang, Y. Liu, G. Zhou, S. Xu, F. Zhang, H. Zhu, F. Liu, and X. Zhu, Revealing the critical role of the HOMO alignment on maximizing current extraction and suppressing energy loss in organic solar cells, IScience **19,** 883 (2019).

[87] C. Yang, J. Zhang, N. Liang, H. Yao, Z. Wei, C. He, X. Yuan, and J. Hou, Effects of energy-level offset between a donor and acceptor on the photovoltaic performance of non-fullerene organic solar cells, J. Mater. Chem. A **7,** 18889 (2019).